Mouslopoulou, V., Oncken, O., Hainzl, S., Nicol, A. (2016): Uplift rate transients at subduction margins due to earthquake clustering. - *Tectonics*, *35*, 10, pp. 2370—2384.

DOI: http://doi.org/10.1002/2016TC004248

AGU PUBLICATIONS

Tectonics

RESEARCH ARTICLE
10.1002/2016TC004248

Key Points:
- Transient uplift rates along fore-arc settings due to earthquake clustering
- Earthquakes nucleate mostly on upper plate splay faults and less on the plate interface
- Late Quaternary paleoshorelines may provide seismic hazard information along seismically quiet subduction margins

Supporting Information:
- Supporting Information S1
- Table S1
- Supporting Information S2

Correspondence to:
V. Mouslopoulou,
vasso@gfz-potsdam.de

Citation:
Mouslopoulou, V., O. Oncken, S. Hainzl, and A. Nicol (2016), Uplift rate transients at subduction margins due to earthquake clustering, *Tectonics*, *35*, 2370–2384, doi:10.1002/2016TC004248.

Received 21 MAY 2016
Accepted 17 AUG 2016
Accepted article online 23 AUG 2016
Published online 18 OCT 2016

Uplift rate transients at subduction margins due to earthquake clustering

Vasiliki Mouslopoulou[1], Onno Oncken[1], Sebastian Hainzl[1], and Andrew Nicol[2]

[1]German Research Centre for Geosciences, GFZ Helmholtz Centre Potsdam, Potsdam, Germany, [2]Department of Geological Sciences, University of Canterbury, Christchurch, New Zealand

Abstract Coastal uplift is common in continental fore-arc systems, with elevated paleoshorelines indicating that uplift rates can vary dramatically over time on individual margins. The origins of these changes in uplift rates are examined using a global data set of paleoshorelines together with 2-D numerical models of subduction systems. Empirical paleoshoreline data ($N = 282$) from eight subduction margins indicate that uplift rates are generally not steady state and varied by up to a factor of 20 during the late Quaternary (≤125 ka). On many subduction margins uplift rates increase to the present day, a finding which we attribute to sampling bias toward those locations where Holocene uplift rates have been highest (with respect to other global margins which have undergone fast subsidence or no vertical motion—e.g., a property akin to the so-called Sadler effect). Paleoshorelines and 2-D models suggest that transient uplift rates at subduction margins are mainly a short-term (<20 ka) phenomenon that cannot be accounted for by plate-boundary scale processes such as changes in the rates of plate convergence, sediment underplating or isostatic unloading. Instead, time-variable uplift rates are ascribed to temporal clustering of large-magnitude earthquakes on upper plate faults and, to a lesser extent, the subduction thrust. The potential for future damaging earthquakes and tsunamis may have been underestimated at active subduction margins with no measureable Holocene uplift, and in such cases, late Quaternary paleoshorelines could provide an important constraint for hazard analysis.

1. Introduction

On million year timescales, coastal uplift appears to dominate vertical motion of terrestrial fore-arc regions for both accreting and eroding subduction systems [e.g., *Savage*, 1983; *Tichelaar and Ruff*, 1993; *Lallemand et al*., 1994; *Nicol and Beavan*, 2003; *Wang*, 2007]. On the timescale of a subduction thrust seismic cycle, which is most often hundreds to thousands of years, vertical motion of the emergent continental fore-arc varies in sign depending on its precise location with respect to the zone of seismic (or aseismic) slip on the subduction thrust [e.g., *Savage*, 1983; *Wang*, 2007] (Figure 1a). While this short-term behavior is mostly elastic and largely recovered during the seismic cycle (Figure 1a), long-term (e.g., ≥125 ka) permanent uplift of emergent fore-arcs may be driven by a variety of seismic and aseismic mechanisms, including slip on the subduction thrust or fore-arc faults (Figures 1b and 1c), slab unloading due to subduction erosion of the upper plate, sediment underplating, and subduction of oceanic topography (e.g., seamounts and spreading ridges) (Figure 1d) [*Lallemand et al*., 1992; *Fisher et al*., 1998; *Wilson et al*., 2007]. These processes occur over a range of temporal and spatial scales and analysis of permanent uplift at subduction margins may provide valuable information about the primary origins of this uplift and of related plate-boundary seismogenesis [e.g., *Melnick et al*., 2009; *Victor et al*., 2011].

Paleoshorelines can constrain the magnitude and mechanisms of coastal uplift along emergent fore-arcs [e.g., *Pirazzoli et al*., 1996; *Mouslopoulou et al*., 2015a]. These ancient coastlines can be spectacularly preserved as wave-cut platforms, benches, and sea notches and provide a geological record of the interplay between eustatic sea level changes and rock uplift relative to the geoid [e.g., *Laborel et al*., 1994; *Pirazzoli et al*., 1996]. In fore-arc regions worldwide (e.g., Kamchatka, Japan, New Zealand, Papua New Guinea) average Holocene rates of vertical uplift are generally higher (e.g., ≥10 times) than for time intervals of ≥125 ka [e.g., *Ota*, 1986; *Berryman*, 1993; *Pinegina et al*., 2013; *Meghraoui et al*., 2013; *Pedoja et al*., 2014]. This variability in uplift rates is not widely addressed in the literature, although some [*Pedoja et al*., 2014, and references therein] attribute it to errors associated with the altitude/age measurements of the uplifted paleoshorelines coupled with the variability of the sea level curve, while others [*Bloom*, 1980; *Ota and Yamaguchi*, 2004; *Shaw et al*., 2008; *Meghraoui et al*., 2013; *Pedoja et al*., 2014] ascribe it to Holocene increases in the convergence

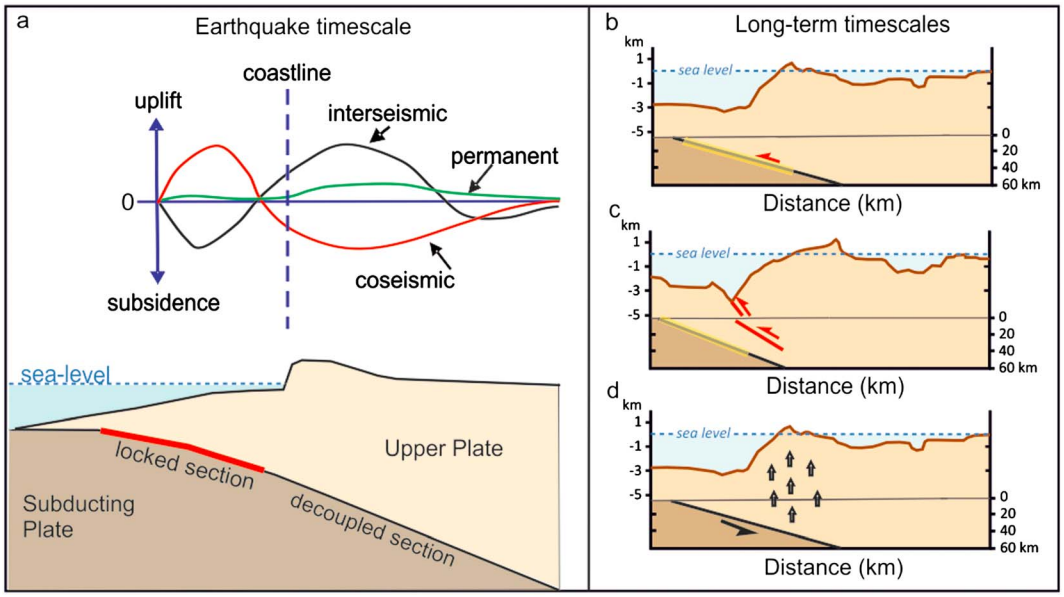

Figure 1. (a) Schematic diagram illustrating the distribution of vertical motion in a fore-arc of a subduction margin during an earthquake cycle. Long-term (≥125 ka) accumulation of vertical uplift may be achieved by (b) slip along the plate interface, (c) slip on upper plate reverse faults, and/or (d) due to aseismic deformation. See text for discussion.

rates and associated changes in the frequency of earthquakes. While uplift rates are strongly censored by eustatic changes in sea level, with values above the blue dashed line in Figure 3 required to outpace rising sea level [e.g., *Siddall et al*., 2003] and produce subaerial exposure of paleoshorelines, such censoring is unlikely to generate the observed rate variations. Similarly, increases in convergence rates require acceleration of plate velocities, which are not supported by field observations [*Gardner et al*., 1987; *Nicol et al*., 2009] or measurements of plate motions over different timescales [*Beavan et al*., 2002; *De Mets et al*., 2010]. Instead, Holocene acceleration of uplift rates may be due to the "Sadler effect" [*Sadler*, 1981], which has been widely observed in geological systems and arises from a combination of variable process rates and preferential sampling of components of the system that experienced the highest Holocene rates [*Sadler*, 1981; *Gardner et al*., 1987; *Sadler*, 1994, 1999; *Jerolmack and Sadler*, 2007; *Nicol et al*., 2009; *Willenbring and von Blanckenburg*, 2010; *Sadler and Jerolmack*, 2014; *Kemp and Sadler*, 2014; *Gallen et al*., 2015]. Independent of the origin of the apparent acceleration of Holocene uplift rates at subduction margins, it is clear that these rates are temporally variable. The focus of this paper is to quantify these variations and elucidate the underlying processes.

Here we use paleoshorelines and numerical modeling to examine the magnitudes and origin(s) of temporal variations in uplift rates on subduction margins worldwide. Order-of-magnitude temporal fluctuations in fore-arc uplift rates are observed using 282 uplifted paleoshorelines spanning 1 ka to ~10 Ma in age from eight subduction margins globally (Calabrian, Italy; eastern and western Hellenic, Greece; Hikurangi, New Zealand; north Honshu-Hokkaido, Japan; Huon Peninsula, Papua New Guinea; eastern Makran, Iran-Pakistan; and southern Chilean, South America) (Figure 2 and Table 1; see supporting information Table S1 for the values, including uncertainties, and the sources of each uplift rate). Comparison of the paleoshoreline data with output from 2-D numerical subduction system models indicates that temporal variations in uplift rates can be produced by changes in the displacement rates of upper plate faults and subduction thrusts. In the models, transient uplift rates are primarily generated by coseismic uplift associated with temporal clustering of large-magnitude earthquakes, followed by long periods (relative to the average recurrence interval) of seismic quiescence. Given the size and geographical extent of our data set the conclusions of this paper are likely to have wide application.

2. Empirical Uplift Rate Transients

The margins studied span a range of convergence rates (Calabria ~5 mm/a to Japan ~90 mm/a) and subduction styles (e.g., from tectonic accretion to tectonic erosion), with coastlines located from ~60 to 320 km from

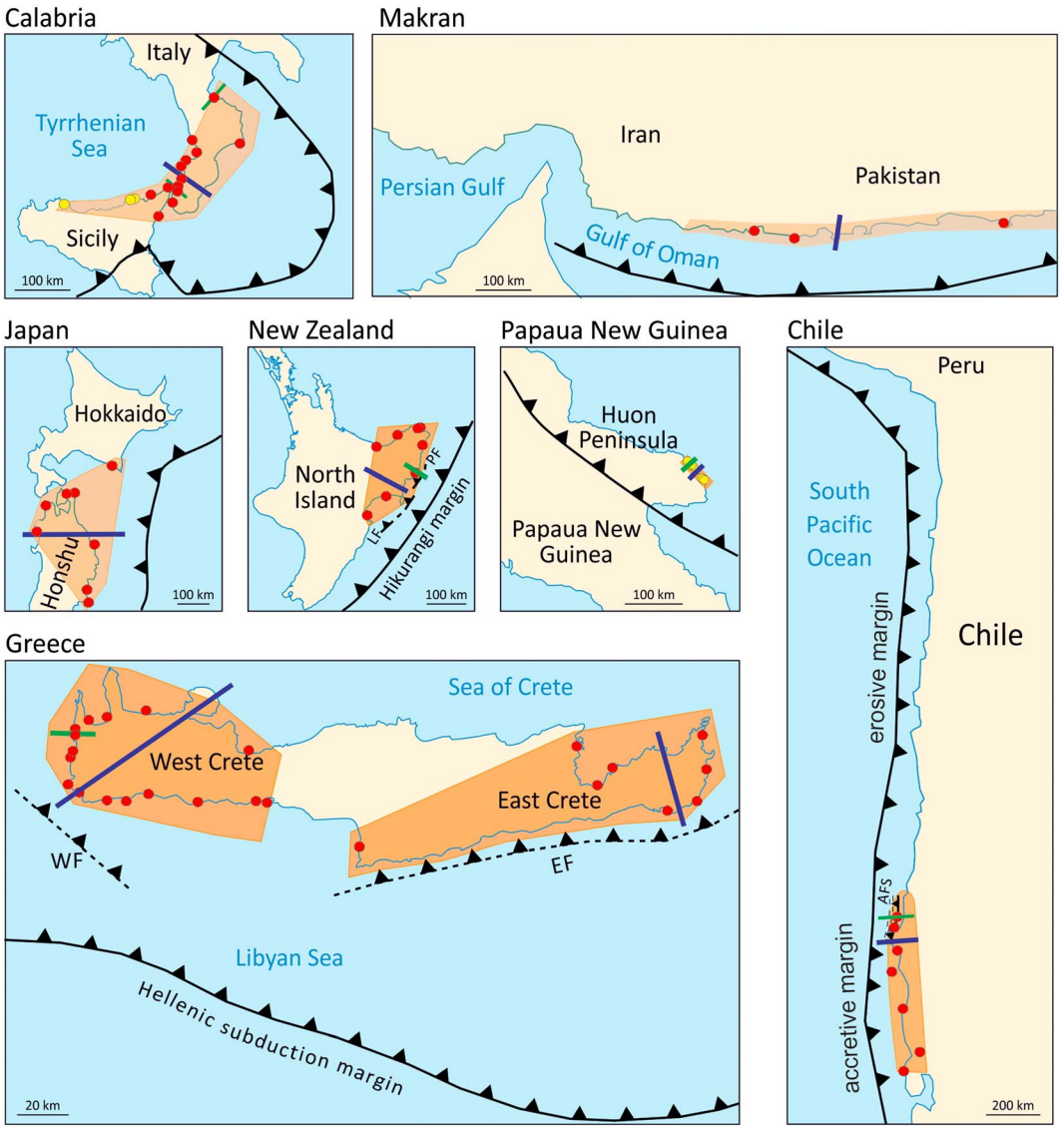

Figure 2. Locality map illustrating the subduction margins discussed in this study. The extent of each fore-arc examined is highlighted by orange polygon, while red filled circles indicate the individual uplift rate localities. Yellow filled circles in Calabria and PNG reflect data points recording current uplift due to collision. Green lines show the location of the individual transects presented in Figure S2. Dark blue lines on each margin show the location of the across-strike profiles presented in Figure S3. LF = Lachlan Fault and PF = Pakarae Fault (New Zealand), WF = Western Fault and EF = Eastern Fault (Greece), and AFS = Arauko Fault System (Chile).

the trench, while the length of each fore-arc examined in most cases exceeds 100 km (Table 1). Despite the geometric and kinematic complexities along each fore-arc which can produce subsiding or uplifting crustal blocks, here we focus only on fore-arc sections that experience uplift. All margins but one, that of Papua New Guinea, are currently experiencing uplift due to subduction of oceanic crust beneath continental crust. The fore-arc of Papua New Guinea (PNG) is currently experiencing uplift due to collision [*Cooper and Taylor*, 1987].

Short-term (<20 ka) temporal variations (0–7 mm/a) in coastal uplift rates and uniform long-term (≥125 ka) uplift rates of ~1 ± 0.75 mm/a have been observed on all sections of the plate boundaries examined (Figure 3). For six of these margins, Holocene (0–10 ka) uplift rates are up to an order-of-magnitude greater than late Quaternary (0–125 ka) rates (Figure 4a). On the remaining two margins (eastern Crete and Makran) no measurable uplift was recorded during the Holocene (Figures 3 and 4a), although their 10–25 ka uplift rates were up to 6 mm/a

Table 1. Summary of the Main Tectonic and Geographic Characteristics of the Margins Examined[a]

Margin	No. of Data Points	Locality	Country	Convergence Rate (mm/a)	Uplift Rate (mm/a) (min-max)	Uplift Rate (mm/a) (min-max)	Uplift Rate (mm/a) (min-max)	Uplift Rate (mm/a) (min-max)	Length of fore-arc Examined (km)	Distance From the Trench
					Holocene (0–10 ka)	15 ± 5 ka	0–125 ka	>500 ka		
Hellenic	87	West Crete	Greece	35–40	1,5-6,7	4,8-6,5	-	0,5-0,8	100	~250
Hellenic	20	East Crete	Greece	35–40	0	2,6	0,3-0,6	0,3-0,4	140	250–300
Calabrian	44	Sicely/Calabria	Italy	~5	1,4-2,4	-	0,2-1,2	0,2-1,1	250	70–300
Chilean	36	37–42° N	Chile	66	1,8-5,4	-	0,03-0,6	0,03-0,6	600	60–150
Hikurangi	49	North Island	New Zealand	45	2-3,8	-	0,4-0,9	0,002-0,9	250	60–150
Japan	16	Northeast Japan	Japan	90	0,8-4,3	-	0,1-0,4	0,15-0,2	400	200–320
Papua New Guinea	22	Huon Peninsula	Papua New Guinea	82	2,2-4,8	-	2,7-3,5	1-1,7	50	60–80
East Makran	8	Gulf of Oman	Iran-Pakistan	~23	0	2,4-4,4	0,1-0,3	0,1-0,3	900	100–150

[a]Convergent rates are from *McCaffrey* [1997], *Abbott et al.* [1997, and references therein], *Wallace et al.* [2004], *D'Agostino and Selvaggi* [2004], *Masson et al.* [2007], *Moreno et al.* [2010], and *Vernant et al.* [2014].

(Figure 3). However, at margins where high uplift rates are observed for the Holocene, the rates may not have been constantly high throughout the Holocene. For example, in western Crete the rate decreased to <1 mm/a during 2–5 ka before climbing to the present rate of ~6–7 mm/a (Figure 3) [*Mouslopoulou et al.*, 2015a]. These uplift rate transients persist for slow (e.g., Calabria, Hellenic, and Makran) and fast (e.g., Japan, Chile, and PNG) converging margins (Figure 4a and Table 1); however, their amplitude (scatter) generally scales linearly with increasing convergence rate (see Figure 4b), a property that mainly reflects the fact that the lower bound of uplift rates is zero in all cases and the upper bound rises with increase in convergence rate. Our data set shows that variable Holocene uplift rates and uniform late Quaternary (>125 ka) uplift rates are independent of regional factors such as interface dip, distance from the trench, and coastline location relative to the interseismically locked zone on the plate interface (Table 1) [*Wang*, 2007], indicating that the uplift is strongly influenced by local processes.

The associated geographical spread of uplift measurements, along and across each margin, could influence the results if there were spatial variations in the uplift rates and the ages of marine terraces. To test whether the inclusion of spatially distant along-margin uplift rate measurements (supporting information Figure S1) could influence our first-order conclusions, we compare uplift rates from six narrow (<10 km) transects on five of the margins studied (see green lines in Figure 2 and supporting information Figure S2) with those from the margin-wide distributions (Figure 3). This comparison shows that uplift rates from the individual transects (supporting information Figure S2) closely match the uplift patterns from the corresponding margin-wide sections (Figure 3), indicating that our data sets may be used as a proxy to derive first-order conclusions on the uplift rate variability on fore-arc settings. The impact of the along-strike variability can be also shown quantitatively on western Crete, where the variability due to heterogeneous slip during the A.D. 365 earthquake (up to 3 mm/a) [*Pirazzoli et al.*, 1996] accounts for <40% of the recorded temporal variability (8 mm/a) in the uplift rates of western Crete (Figures 3 and 4a). Thus, although spatially heterogeneous coseismic slip along each margin may locally impact uplift rates, it cannot explain the order-of-magnitude temporal variability recorded here.

The across-strike variability is tested on each margin by plotting the uplift rates, averaged over two different time intervals (0–25 ka and > 25 ka), as a function of the distance across the fore-arc (supporting information Figure S3). In all cases, the data underscore the fact that Holocene rates are higher than longer-term late Quaternary rates (supporting information Figure S3). This

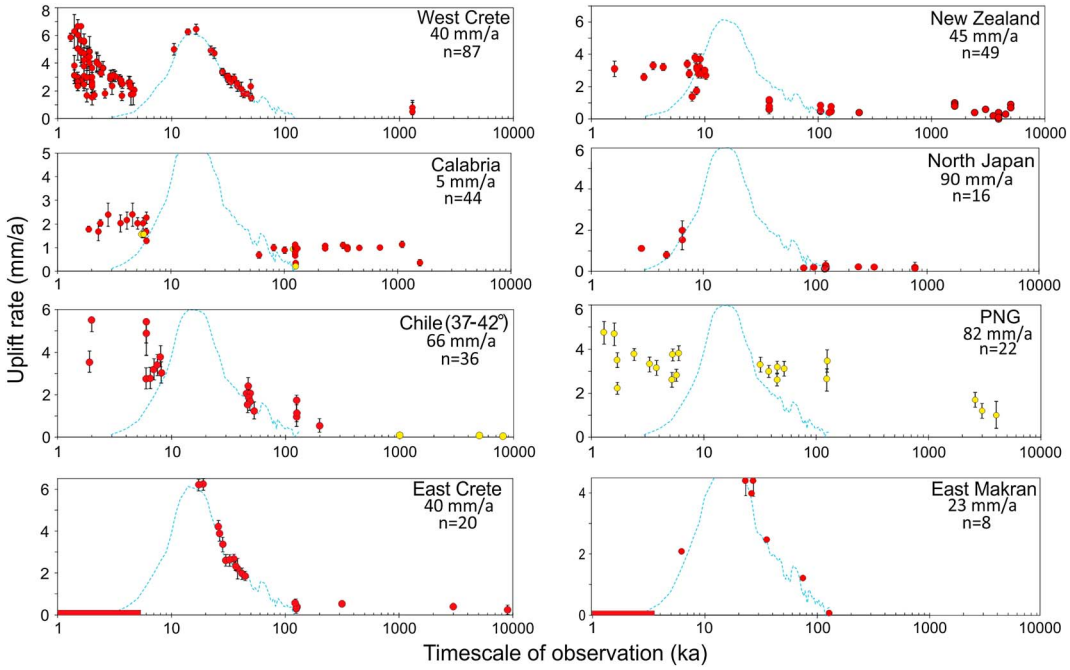

Figure 3. Fore-arc uplift rates as a function of time for eight subduction margins. Blue dashed line indicates uplift rates required to outpace rising sea level (using the curve of *Siddall et al*. [2003]). Horizontal bars during late Holocene for east Crete and west Makran margins reflect no measurable uplift with respect to sea level. The convergence rate and the number of data points in each data set (*n*) are indicated. Yellow filled circles in Calabria and PNG reflect data points that currently record uplift due to collision, while in Chile they record exhumation rates. See supporting information Table S1 for each uplift rate value and its source.

in turn indicates that the rate variability persists across the entire margin and is not only associated with individual localities. Analysis of supporting information Figure S3 also shows that in several cases there is a trend toward decaying uplift rates landward. This gradient is more pronounced in some studied margins (e.g., Chile, western and eastern Crete, Makran, and PNG) than others, where across-margin uplift appears to be more constant (e.g., Calabria and New Zealand). The former likely reflects that uplift is controlled by a single master fault (e.g., the WF and EF in western and eastern Crete, respectively; Figure 2), whereas the latter reflects either distributed shortening over a wider area or a larger number of closer spaced smaller faults that prevent a single gradient (e.g., see LF and PF structures in New Zealand; Figure 2). A landward gradient of long-term uplift rates is expected given that the maximum uplift is concentrated above the downdip end of the zone of seismic coupling which globally tends to be below the coastline [*Tichelaar and Ruff*, 1993] (Figure 1b). Numerical simulations and analog experiments [*Rosenau et al*., 2009] have shown that this is a consequence of stress concentration at the downdip end of the locked zone, causing the hanging wall immediately above to deform and uplift (i.e., initially, uplift occurs across a broad diffuse zone and gradually, over hundreds of seismic cycles, it localizes onto more discrete structures). Further, the data in supporting information Figure S3 show that the lateral variability recorded along each of the studied fore-arcs (e.g., supporting information Figure S1), when collapsed onto a single across-margin transect, does not fundamentally impact on the uplift rate variability documented in Figure 3.

Our analysis shows that the fore-arc of PNG experiences higher long-term (>125 ka) uplift rates compared to the long-term rates on the remaining margins examined (Figure 3). We suggest that this is because PNG is currently experiencing collision [*Cooper and Taylor*, 1987]. The collision between the Woodlark and the South Bismarck plates enhances vertical movement which is, in turn, reflected in the elevated uplift rate measurements. Such an effect has also been recorded on eastern Taiwan (see supporting information Figure S4) where very high uplift rates reflect the collision between the Philippines and the Eurasian plates [*Suppe*, 1981]. Despite the effect of collision, it is clear for both margins that Holocene uplift rates are faster than their corresponding late Quaternary rates (Figure 3 and supporting information Figure S4).

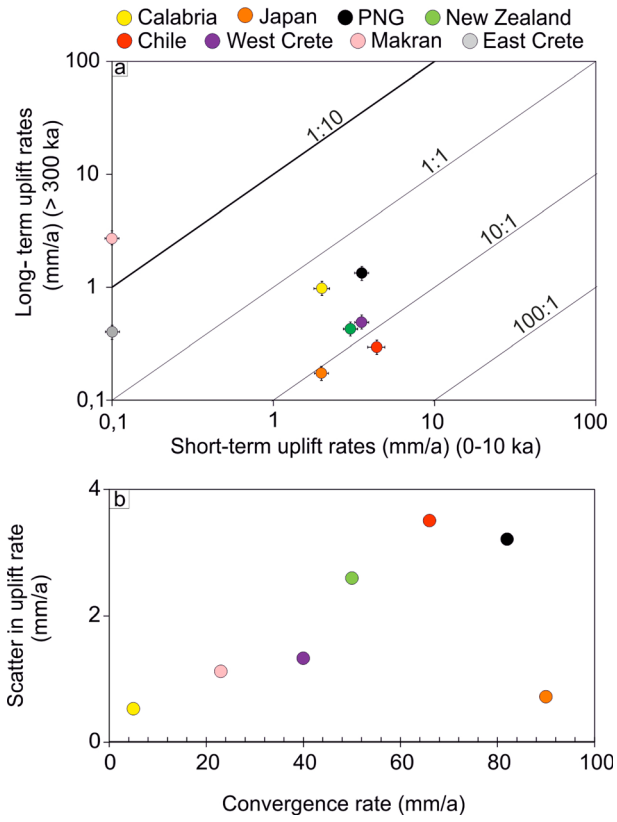

Figure 4. (a) Uplift rates averaged over 300 ka are compared, for each subduction margin, with their corresponding 0–10 ka uplift rates. (b) The scatter in uplift rates for each margin is plotted as a function of the margin's convergence rate. Scatter is defined as the difference between the average short-term (<20 ka) and long-term (>300 ka) uplift rate on each margin, corrected for its distance from the trench (all values are normalized to an average distance of 100 km).

The temporal variability of uplift rates decreases on all margins with increasing duration of the sample interval (Figure 5a), consistent with the view that fast rates of episodic processes are not sustained for long time periods (e.g., variability is expected to diminish within the timescales of their unsteadiness as averaging time increases) [*Strauss and Sadler*, 1989; *Sadler and Strauss*, 1990; *Sadler and Jerolmack*, 2014]. In Figure 5a, uplift rates from all margins have been normalized and compared using an index of variability $I = (UR - UR_L)/UR_L$, where UR = uplift rate at each fore-arc locality and UR_L = average long-term (≥300 ka) uplift rate at each margin. Indeed, comparison suggests that the variability in uplift rates is maximum for all margins over time intervals that span ~0–10 ka and decreases with increasing size of time window to become negligible for time intervals >125 ka. Subduction thrust processes that could play a role in uplift of fore-arc systems, such as isostatic unloading due to subduction erosion, sediment underplating, subduction of seamounts and oceanic ridges [e.g., *Lallemand et al.*, 1992, 1994; *von Huene and Scholl*, 1991; *Dominguez et al.*, 1998], typically produce slower and longer-lasting transients and are unlikely to explain the observations (Figure 5b). Glacial isostatic adjustment can locally be quite fast (up to 5 mm/a uplift) for active margins in high-latitude areas [e.g., *James et al.*, 2000] but cannot account for the acceleration of uplift rates in the data sets used here, as they derive from moderate-latitude areas (Figure 2). In addition, accelerated uplift rates are generally not synchronous between margins (Figure 3) and cannot be attributed to global processes, such as increases in plate velocities and/or elevated (or decreased) fault slip arising from changes in global sea level or the direct effect of water loading on stress magnitudes [e.g., *Hetzel and Hampel*, 2005].

Instead, we argue that the Holocene acceleration of rates on some subduction systems reflects a propensity for temporal variations in uplift rates coupled with a sampling bias toward those margins where Holocene uplift has been greatest and paleoshorelines are most likely to be preserved (and observed) above sea level. The property of numerous interruptible and reversible geological processes (such as sediment accumulation rates, incision and/or erosion rates, magma generation rates, aggradation rates, tectonic rates, and denudation and/or progradation rates), to inversely scale with the measured time interval, producing negative power laws (associated with short-lived transients), has been observed empirically and modeled numerically worldwide [*Sadler*, 1981; *Gardner et al.*, 1987; *Sadler*, 1994, 1999; *Jerolmack and Sadler*, 2007; *Sadler and Jerolmack*, 2014; *Kemp and Sadler*, 2014; *Gallen et al.*, 2015]. In Figure 5c we compare the temporal evolution of the uplift rate on each of the studied fore-arcs with distributions from global sediment accumulation rates [*Sadler*, 1999] and fault displacement rates [*Mouslopoulou et al.*, 2009]. Comparison shows that uplift rates on all studied margins produce negative power law distributions with their slope ranging between the slopes produced by the two other data sets (Figure 5c). This fundamental similarity of the observed acceleration of uplift in paleoshorelines with sedimentation rates is an apparent feature that highlights the bias of geological archives that develop incrementally and are subject to

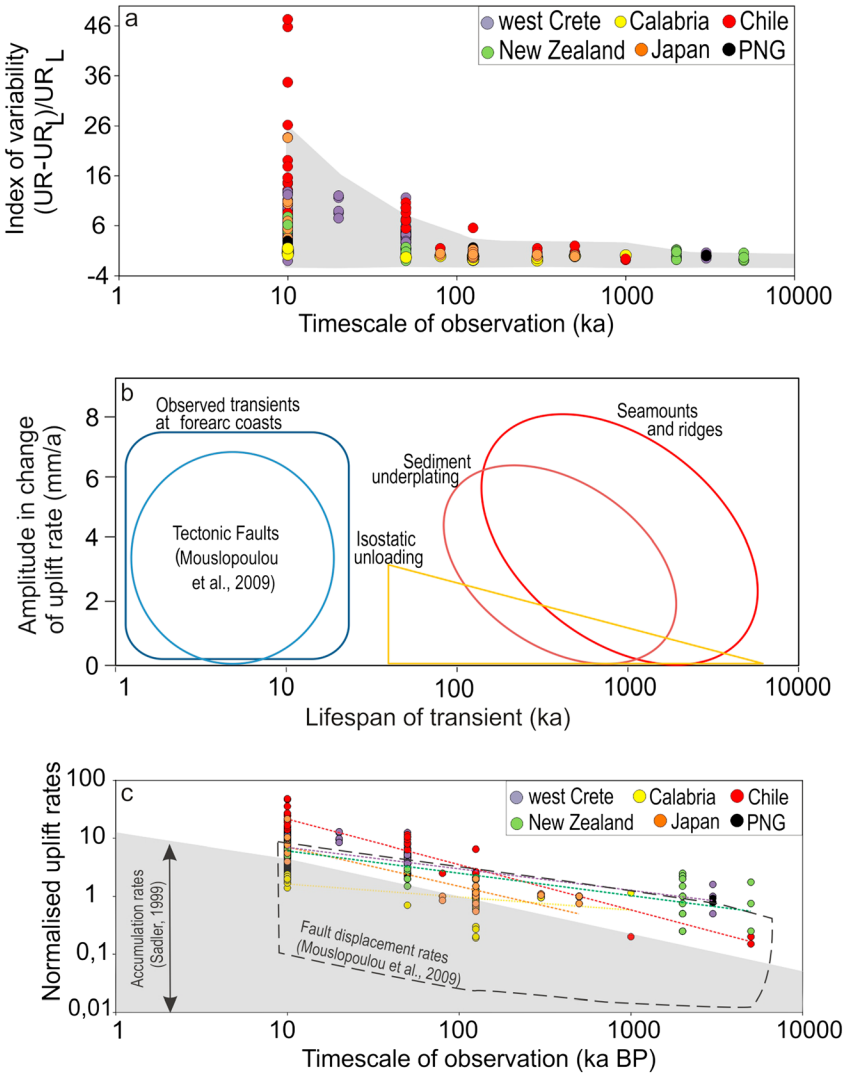

Figure 5. (a) Plot illustrating the index of variability (I) as a function of time for each data set. UR = measured uplift rate at each fore-arc locality; UR_L = average long-term (≥300 ka) uplift rate for each margin. Note that the data are grouped into representative time intervals (e.g., 0–10 ka, 0–20 ka, and 0–50 ka) to facilitate comparison. Shaded area outlines the displacement rate variability recorded by 261 normal and reverse faults globally (from *Mouslopoulou et al.* [2009]). (b) Amplitude and lifetime of typical uplift transients at convergent margins estimated for a range of convergence velocities (20–80 mm/a), thickness of trench fill (200–2000 m), and widths (5–200 km) of subducting elements such as sediments, ridges, seamounts, and isostatic unloading, driven by subduction erosion rate equivalent to trench retreat rate of 1–3 km/Ma [*Lallemand et al.*, 1992, 1994; *von Huene and Scholl*, 1991; *Dominguez et al.*, 1998]. (c) Log-log plot illustrating the temporal evolution of uplift rates on each subduction margin. Grey shaded area represents the distribution of 38,660 empirical measurements of sediment accumulation rates on passive continental margins [*Sadler*, 1999]. The distribution of fault displacement rates [*Mouslopoulou et al.*, 2009] is also plotted (dashed black line) for comparison.

both, formation and destruction, processes. Further, the striking similarity of fore-arc uplift transients to temporal fluctuations in displacement rates on individual faults globally (indicated by the shaded area and the dashed black line in Figures 5a and 5c, respectively) [*Mouslopoulou et al.*, 2009], together with the apparent local source of uplift, leads to the conclusion that upper plate faulting is an important mechanism for generating uplift rate variability at short timescales (<20 ka). Steep reverse faults that splay from the interface into the upper plate beneath the fore-arc are common within convergent margins (e.g., Cascadia, southern Chile, Hellenic, Nankai, Hikurangi, and Sumatra), where they have produced great earthquakes and catastrophic tsunamis that contribute to hazards [e.g., *Park et al.*, 2002; *Rodgers and Little*, 2006; *Shaw et al.*, 2008; *Priest et al.*, 2009; *Singh et al.*, 2011].

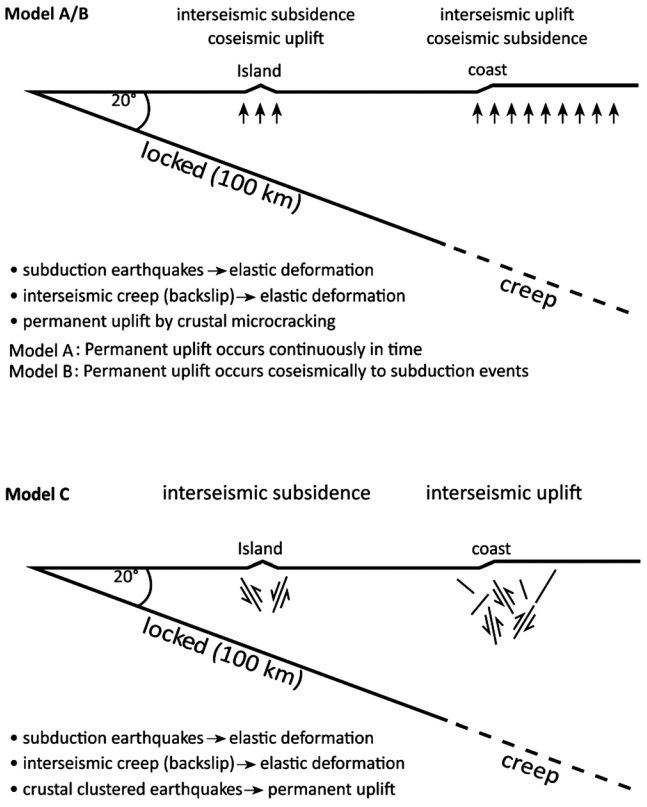

Figure 6. Schematic cross section illustrating the setup of various stochastic numerical simulations of uplift rates on fore-arc settings. While all models are based on elastic deformation due to subduction events and interseismic creep, they differ with regard to the source of permanent uplift: Continuous uplift (Model A), coseismic uplift with subduction events (Model B), and uplift due to crustal earthquakes (Model C). See text for details.

3. Subduction Models and Uplift Rate Variability

To examine the origin of uplift transients, we have constructed simple stochastic models which simulate uplift in fore-arc settings due to repeated earthquakes associated with constant plate convergence. The models are not intended to replicate the geometric/kinematic characteristics of a particular subduction margin but rather use simple assumptions (see below) to help explain the first-order temporal variations in uplift rates recorded by the empirical data on the eight subduction margins.

3.1. Model Setup

Our model setup is based on the back slip model of *Wang* [2007], in which vertical motion results from a combination of coseismic slip and interseismic continuous elastic deformation due to locking on the plate interface. The geometrical setup is shown in Figure 6, where we assumed a constant convergence rate of 40 mm/a and a 100 km wide coupled zone that dips 20° beneath the upper plate (Table 2). Generally we assume that slip in the seismogenic zone is purely seismic (i.e., with a coupling coefficient of 1; however, we also discuss lower coupling values in the following section). For simplicity and computational efficiency, we assume an elastic half-space for which the surface deformation in response to dislocations at depth can be calculated by means of the analytic solutions of *Okada* [1992], where we set the Poisson ratio to 0.25. The resulting coseismic surface uplift/subsidence is illustrated in Figure 7a for two exemplary earthquakes. Deformation during interseismic periods is modeled by continuous back slip of the coupling zone with the convergence rate. The balancing of coseismic slip in the coupling zone is produced by randomly drawn earthquakes ($6 < M_w < 9$) from a Gutenberg-Richter population with a b value of 1. The rate of the temporally random subduction events (a value) is determined by the condition that the average slip rate in the coupling zone is equal to the convergence rate (e.g., 40 mm/a). An exemplary time series of simulated subduction events and corresponding surface deformation is shown in Figures 7b and 7c. However, the main results are found to be stable and independent of the specific choice of convergence rate and/or dip of the subducting slab (see Figures S5, S7, S9, and S11 in the supporting information). For comparison, we also developed slip distributions by assuming quasi-periodic recurrence of characteristic

Table 2. Input Parameters for the Stochastic Numerical Model

Parameters	Values
Dip of slab (deg)	20
Seismogenic width W_{seis} (km)	100
Minimum magnitude	6
Maximum magnitude	9
b value	1
Convergence rate (mm/a)	40
Simulation time (years)	10^7

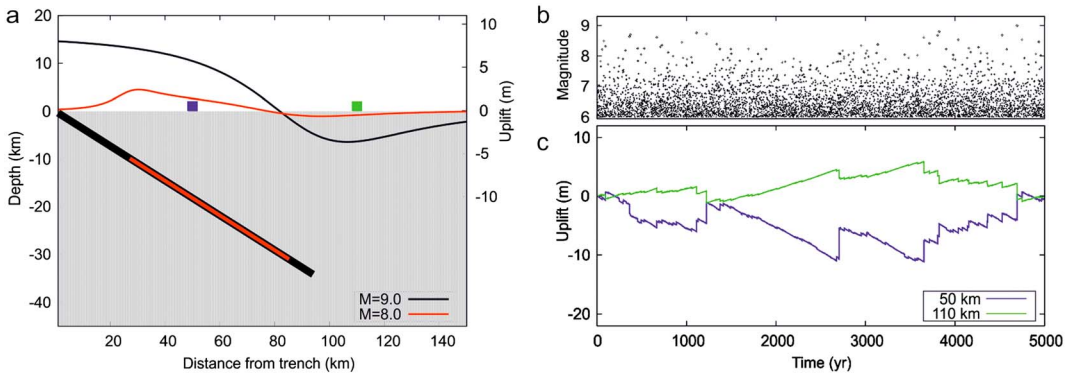

Figure 7. Examples of simulated subduction earthquakes at an interface with dip = 20°: (a) Coseismic surface uplift in response to exemplary magnitude 8 and 9 events, respectively. (b) Time series of earthquakes occurring randomly in time with magnitudes distributed according to a Gutenberg-Richter distribution between 6 and 9 with $b = 1$. (c) Uplift time series at the two locations marked in Figure 7a due to coseismic uplift related to events in Figure 7b and interseismic back slip.

earthquakes according to the Brownian-Passage-Time (BPT) distribution [*Matthews et al.*, 2002]. The results of the BPT model lead to conclusions similar to those based on the Gutenberg-Richter distribution and are described in the supporting information (see Figures S6 and S10).

The extent of the subduction zone in strike direction is set to be slightly larger than the average length of the M_{max} event, that is, 600 km for $M_{max} = 9.0$. The uplift histories are measured at the ground surface in the center of the modeled margin. For each earthquake, the rupture location is randomly distributed within the coupling zone of the subduction interface; the length (L) and width (W) of the earthquakes are randomly selected from empirical distributions for reverse earthquakes of a given magnitude [*Blaser et al.*, 2010], provided that the rupture extends within the coupling zone. The corresponding average slip value is determined by the seismic moment magnitude (M_w) and rupture area (LW) according to $d = 10^{1.5M_w + 9.1}/(\mu LW)$, assuming a shear modulus of $\mu = 35$ GPa. For computational efficiency, we assume uniform slip, although real slip distributions are known to be heterogeneous [*Mai and Beroza*, 2002]. All specific model parameters are summarized in Table 2.

For the accumulation of permanent fore-arc deformation we consider three alternative models (see Figure 6):

1. Permanent uplift is accumulated continuously in time due to microcracking (aseismically) leading to distributed fore-arc deformation (Model A).
2. Permanent uplift occurs coseismically as a certain percentage (e.g., 5–20%) of the absolute value of the elastic vertical surface deformation related to plate interface subduction earthquakes (Model B).
3. Permanent uplift is due to upper plate crustal earthquakes which are Gutenberg-Richter distributed and clustered in time (Model C). Because such fore-arc fault systems are often associated with along-strike geometric complexities, here we do not model any specific fault network. Instead, we consider a simplified generic case, where the sizes of uplift increments are taken from a probability distribution rather than calculated for specified earthquake mechanisms and locations. In particular, we assume (i) a Gutenberg-Richter distribution of the earthquake magnitudes and (ii) a linear relation between the seismic moment of earthquakes and their induced permanent uplift of the surface, which would be exactly valid for point sources with a specific mechanism and depth. By means of this approximation, the distribution of uplift values and the activity rate is constrained by the maximum possible uplift (u_{max}) which corresponds to the largest crustal event, the average (permanent) uplift, the b value, and the magnitude difference ΔM between the largest and smallest modeled crustal events. Here we assume $u_{max} = 10$ m, $b = 1$, and $\Delta M = 4$. Smaller maximum uplift (u_{max}) values lead to similar results, with the exception of the time period between 10 and 30 ka where terraces are less frequently (if at all) observed above sea level (see Figures S8 and S12 in the supporting information).

   The temporal earthquake occurrence of the crustal events is described by the epidemic-type aftershock sequence (ETAS) model, which is currently the standard statistical model for crustal seismicity [*Ogata*,

1988; *Zhuang et al*., 2012]. In this model, tectonic earthquakes occur at times t_i according to a Poissonian process with rate r and earthquake-earthquake interactions lead to additional aftershock activity according to the Omori law.
The total activity rate R is described by

$$R(t) = r + \sum_{i:\, t_i < t} K 10^{\alpha M_i} (c + t - t_i)^{-p}$$

In our simulations, we choose typical coefficients $c = 0.01$ days, $p = 1.2$, $\alpha = b = 1$, and constrain K by the condition that the aftershock fraction is on average 80%. In the supporting information, we show that the results remain unaffected for other coefficient combinations (see Figure S8).

The average value of the permanent uplift is modeled as 0.5 or 1 mm/a in line with empirical long-term observations. Based on these model parameters, we simulate individual uplift histories for time periods of 10^7 years resulting from elastic and permanent deformations. However, measured deformation at the ground surface is censored by sea level fluctuations. This means that paleoshorelines are observable only in circumstances where uplift rates are sufficiently high to outpace interglacial sea level rise [*Siddall et al*., 2003] and to produce present subaerial exposure of paleoshorelines (i.e., they can be routinely observed).

3.2. Origins of Uplift Rate Variability

The observed short-term (<20 kyr) uplift rate transients are inconsistent with steady state aseismic deformation of subduction thrusts or long-lived transients that may be produced by, for example, sediment underplating or other related processes (Figures 1d and 5b). The three models presented (A, B, and C) provide a basis for constraining the origins of the temporal variability in uplift rates (mean values and standard deviations). Indeed, the temporal variability of uplift rates observed at different model simulations over a range of sample intervals (e.g., from 1 to 1000 ka) are shown by the grey shaded areas in Figure 8. Without the filtering of the data by the condition that the marine terrace is above sea level, the uplift record for each model is similar to a random walk with drift, where the standard deviation (σ) of the uplift rates ($u(T)/T$) decreases with $1/\sqrt{T}$ (Figure 8a). This fits well the decay of the standard deviations for constant sea level and also, partly, with the result in the case of real sea level changes (Figure 8b). Although the standard deviations of all models have the same trend, Model C leads to the highest absolute values of the standard deviations because of the temporal clustering of crustal events over short time intervals (Figure 8a). The time dependence of the mean uplift rates is due to this variability in conjunction with sea level filtering.

Models A (aseismic uplift) and B (uplift due to subduction thrust seismic slip) produce similar results, with neither model (Figures 8a and 8b) reproducing the short-term transients in uplift rates recorded by the empirical data (Figure 3). Model C (uplift due to seismic slip on upper plate faults) produces variability in uplift rates which is greater than Models A and B (Figure 8) forcing the uplift rate to exceed the rising sea level during the time interval 10–30 ka in some of the simulations. Specifically, the variability in uplift rates in Models A and B is insufficient to maintain marine terraces above sea level, particularly during the period of rapid sea level rise in the last 20 kyr. For example, Model B produces Holocene acceleration of up to a factor of 5 (compared to long-term >125 ka rates) with maximum uplift rates of ~5 mm/a which are insufficient to produce subaerial exposure of paleoshorelines ~10–30 ka in age, resulting in the broken green line in Figure 9.

By contrast Model C can produce peak uplift rates sufficiently high to outstrip sea level rise and would, for example, have the potential to be recorded on east and west Crete and Makran margins between 10 and 30 ka (Figure 3 and Model C in Figure 8b). The match of output from Model C with paleoshoreline observations is facilitated by addition of seismic slip on the subduction thrust. This seismic slip becomes clear in simulations with smaller seismic coupling coefficients, i.e., when a portion of slip in the seismogenic zone is accommodated by continuous creep. For Model C, in the absence of thrust slip (zero coupling) strong transients are still achieved, with uplift rates of up to ~8 mm/a that would maintain subaerial exposure of paleoshorelines between ~10 and 30 ka; however, the observed Holocene acceleration is only partly achieved with average values mainly between 1 and 2 mm/a (see red line in Figure 9). In addition, the

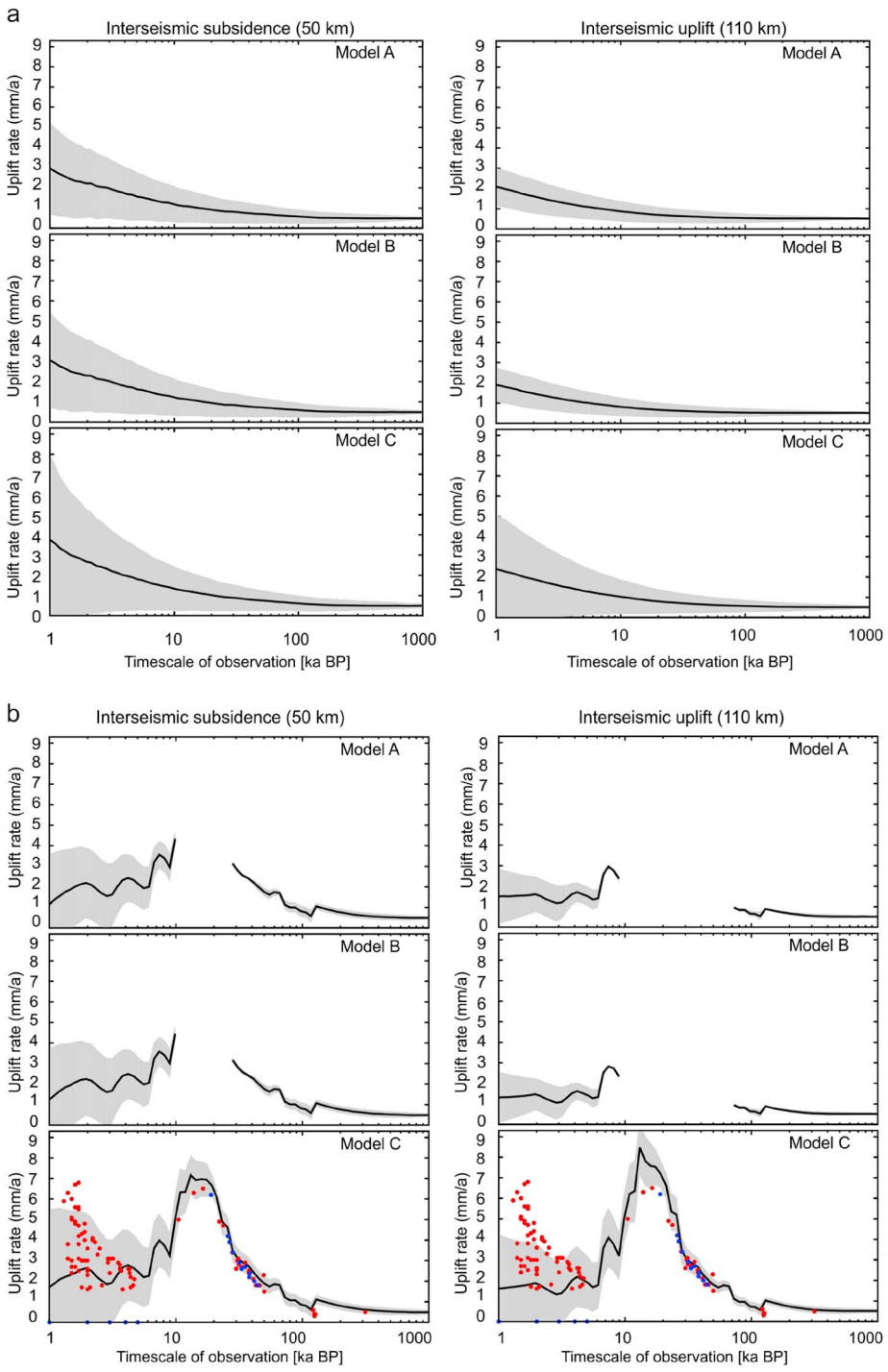

Figure 8. The evolution of average uplift rates through time for Models A, B, and C based on Monte Carlo simulations assuming (a) constant sea level and (b) taking into account the known sea level fluctuations during the last 125 ka [*Siddall et al.*, 2003] (e.g., uplift of observable paleoshorelines have to exceed the known sea level changes). The left column illustrates results for fore-arc coastlines located 50 km from the trench (representing the case of interseismic subsidence), whereas the right column refers to fore-arc coastlines located 110 km from the trench (representing interseismic uplift). The solid line refers to the average value, while grey shaded areas represent the results within (±) one standard deviation. The results of Model C, taking into account the sea level fluctuations and using an average permanent uplift rate of 0.5 mm/a, are compared with the empirical uplift rates measured along the fore-arc of the Hellenic subduction margin on western (red circles) and eastern (blue circles) Crete.

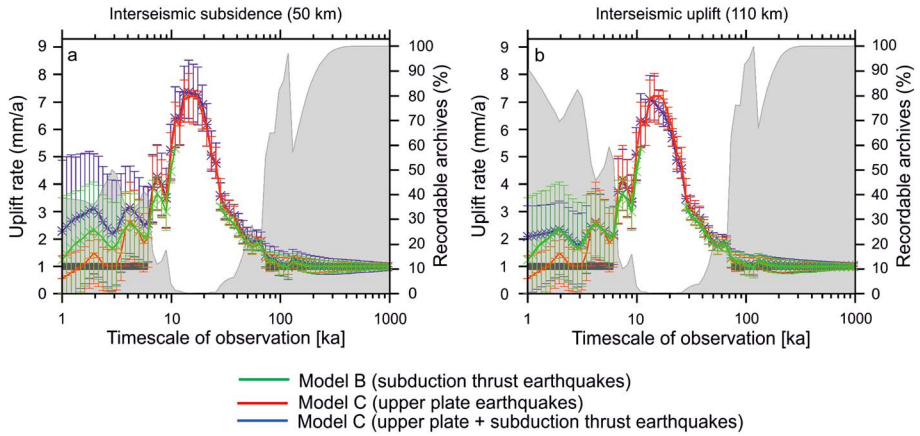

Figure 9. Numerical modeling illustrating uplift rates, and their uncertainties, through time due to plate interface earthquakes (Model B, green line), upper plate earthquakes (red line), and a combination of plate interface and upper plate faulting (Model C, blue line) on fore-arc coastlines located (a) 50 km and (b) 110 km from the trench, respectively. The error bars are at (±) one standard deviation and refer to the variability for different model runs for the same sample location. Grey areas represent the probability corresponding to Model C (blue line) that the archive (e.g., paleoshoreline) will be observed at a given time window. Black horizontal line reflects the uplift rate due to continuous aseismic slip. In all cases, we assumed an average permanent uplift rate of 1 mm/a.

relatively small variance bars in Figure 9 (red line) indicate that Model C (without thrust slip in the interface) does not reproduce the empirical variability in Holocene uplift rates particularly at timescales of <4 ka. A version of Model C that includes moderate to great earthquakes ($M5$ to $M>8$) on upper plate faults and the subduction thrust, most closely replicates (see blue lines in Figure 9) the empirical data which include severe short-term (<20 ka) transients, sufficiently high uplift rates to maintain some paleoshorelines above sea level from 10 to 30 ka, and stable long-term (>125 ka) rates of uplift. However, the likelihood of recording paleoshorelines of ages around 15 ka is $<1\%$ in the simulations (see grey shaded area in Figures 9 and S9–S12 in the supporting information), and thus, such paleoshorelines are expected to be rarely observed on subduction margins. Hence, the apparent synchronicity of sea level motion with uplift transients in some cases (i.e., Crete and Makran) is a consequence of higher variability of earthquake-related uplift pulses in the upper plate and "filtering" of the geological record by subsequent reoccupation of most paleoshorelines by the sea, leaving few that survive. This significant variability generated in Model C with subduction thrust seismic slip results from clustered earthquakes (i.e., with epidemic-type aftershock sequences) on upper plate faults and nonperiodic earthquakes on the subduction thrust.

In summary, modeling supports the view that uplift transients in natural data sets are due to temporal clustering of large-magnitude earthquakes on upper plate reverse faults, aided by nonperiodic rupture on the subduction interface. Stress triggering might also lead to additional clustering of large earthquakes on the subduction thrust and synchronized activity in the overriding plate which is not considered here. However, this type of stress triggering does not seem to be a requirement for the observed uplift rate transients.

4. Discussion

On many subduction margins uplift rates are highest in the Holocene (e.g., Figure 3). Similar rate accelerations toward the present have been recorded for other geological processes, such as the accumulation, aggradation, denudation, progradation, incision, and erosion of fluvial/marine sediments and rocks [*Willenbring and von Blanckenburg*, 2010; *Sadler*, 1981, 1994, 1999; *Jerolmack and Sadler*, 2007; *Sadler and Jerolmack*, 2014; *Kemp and Sadler*, 2014; *Gallen et al*., 2015], and the accumulation of slip on tectonic faults [*Gardner et al*., 1987; *Nicol et al*., 2009]. As uplift is an incremental process such as subsidence, the formation of paleoshorelines is a similar time-dependent process to sediment accumulation, and the time-dependent chance of postformation destruction of paleoshorelines by erosion is the same as the potential sediment removal, we interpret the overall trends in our observations to record the so-called Sadler effect which has been widely reported for sedimentary systems. Specifically, we attribute the temporal variations in uplift rate to the effect of stochastic earthquake clustering, inherent in the process of faulting, superimposed on a

record that is formed incrementally and is subject to destruction. In combination with a tendency to sample margins where uplift rates were greatest during the Holocene, preserved paleoshorelines capture substantial short-term transience with increasing resolution and preservation toward the present.

Thus, the frequently observed acceleration of uplift rates during the Holocene likely reflects temporal clustering of great earthquakes, such as those recorded historically for Sumatra, Cascadia, and western Crete [*Pirazzoli et al*., 1996; *Sieh et al*., 2008; *Goldfinger et al*., 2012; *Kulkarni et al*., 2013], and does not require changes in the rates of plate convergence. The order-of-magnitude variability in displacement rates of upper plate faults and subduction thrusts, a phenomenon which has been observed on normal and reverse faults globally [*Mouslopoulou et al*., 2009] (Figure 5b), results from changes in both the earthquake recurrence interval and the maximum slip of earthquakes [*Marco et al*., 1996; *Nicol et al*., 2006; *Mouslopoulou et al*., 2009]. These changes in the fault displacement rates may be controlled by a number of underlying processes, including temporal changes in frictional properties of the subduction thrust and overlying reverse faults, variability in the degree of locking between the tectonic plates, and/or temporal changes in the strain partitioning between the plate interface and the upper plate faults [*Wech and Creager*, 2008; *Rosenau and Oncken*, 2009].

Seismogenic upper plate reverse faults that splay off the plate interface have been documented on some of the fore-arcs examined here (Figure 2): in eastern and western Hellenic margin [*Shaw et al*., 2008; *Stiros*, 2010; *Mouslopoulou et al*., 2015b], in southern Chile [*Melnick et al*., 2009], and in New Zealand [*Barnes et al*., 2002; *Wilson et al*., 2006]. On some margins (e.g., Hellenic and Hikurangi) these structures coincide with pronounced bathymetric expressions on the ocean floor, while in others (e.g., Chile), these faults appear to be blind. This lack of bathymetric expression indicates that the absence of surface faulting landward of the subduction margin does not exclude the possibility that such faults exist at depth without displacing the ground surface (or the seabed).

The present data set of subduction margins is likely to undersample regions that have experienced little or no Holocene coastal uplift because they preserve no paleoshorelines. Along the eastern Crete and Makran margins, where no Holocene earthquakes or uplift have been recorded, uplift rates were high (5–6 mm/a) during the late Quaternary (10–30 ka) and are here interpreted to indicate current seismic quiescence preceded by a cluster of great earthquakes (Figure 3). The uplift data suggest that the stationarity sampling issues widely attributed to historical seismicity catalogues [e.g., *Rajendran et al*., 2013] also apply on 10,000 year timescales for faults along subduction margins. Given these long-term temporal variations in megaevents and the brevity of the historical earthquake catalogue (e.g., $<$200 years) for many subduction systems globally (e.g., New Zealand, PNG, Chile, and Makran), it is not surprising that on some margins the available data provide few clues to the future seismic potential. Averaged over longer periods of time ($>$20 ka), the majority of megaearthquakes will occur on the fastest-moving ($>$40 mm/a) convergent margins [*Ruff and Kanamori*, 1980], and the potential for underestimating the associated seismic hazard will be inversely related to plate convergence rate. We find that fast (e.g., Chile, Japan, and PNG) and slow (e.g., Calabrian, Makran, and Crete) converging margins are capable of generating large-magnitude earthquakes; however, in circumstances where they are temporally clustered, their rate of occurrence may not be simply related to the long-term ($>$20 ka) rate of convergence. Searching for subduction margins where Holocene uplift is absent and late Quaternary paleoshorelines are preserved may provide a basis for identifying systems where the potential for future large earthquakes has been underestimated (e.g., eastern Crete).

5. Conclusions

Empirical paleoshoreline data ($N = 282$) from eight subduction margins indicate that uplift rates are generally not steady state and varied by up to a factor of 20 during the late Quaternary ($\leq$125 ka). On many subduction margins uplift rates increase to the present day (with respect to other global margins which have undergone fast subsidence or no vertical motion), an artefact that we attribute to sampling bias towards those locations where Holocene uplift rates have been highest (e.g., the so-called Sadler effect). Paleoshorelines and 2-D numerical models suggest that transient uplift rates at subduction margins are mainly a short-term ($<$20 ka) phenomenon that cannot easily be accounted for by plate-boundary scale processes such as changes in the rates of plate convergence, sediment underplating, or isostatic unloading. Instead, transients can be explained by temporal clustering of large-magnitude earthquakes on upper plate reverse faults, aided by nonperiodic rupture on the subduction interface.

Acknowledgments
We thank the reviewers Kelin Wang and Amotz Agnon for their detail and thorough comments that helped improve this manuscript and the Editor Claudio Faccenna for the timely and professional handling of this submission. We also thank Niels Hovius for useful discussions and Chris Goldfinger and Martin Mai for constructive reviews of an earlier version of this article. The reported data, along with their sources, are summarized in Table S1 in the supporting information.

References

Abbott, L. D., E. A. Silver, R. S. Anderson, R. Smith, J. C. Ingle, S. A. Kling, D. Haig, E. Small, J. Galewsky, and W. S. Sliter (1997), Measurement of tectonic surface uplift rate in a young collisional mountain belt, *Nature*, *385*, 501–507.

Barnes, P. M., A. Nicol, and T. Harrison (2002), Late Cenozoic evolution and earthquake potential of an active listric thrust complex above the Hikurangi subduction zone, New Zealand, *Bull. Geol. Soc. Am.*, *114*, 1379–1405.

Beavan, R. J., P. Tregoning, M. Bevis, T. Kato, and C. Meertens (2002), Motion and rigidity of the Pacific Plate and implications for plate boundary deformation, *J. Geophys. Res.*, *107*(B10), 2261, doi:10.1029/2001JB000282.

Berryman, K. R. (1993), Distribution, age, and deformation of late Pleistocene marine terraces at Mahia Peninsula, Hikurangi Subduction margin, New Zealand, *Tectonics*, *12*, 365–1379, doi:10.1029/93TC01543.

Blaser, L., F. Krüger, M. Ohrnberger, and F. Scherbaum (2010), Scaling relations of earthquake source parameter estimates with special focus on subduction environment, *Bull. Seism. Soc. Am.*, *100*, 2914–2926, doi:10.1785/0120100111.

Bloom, A. L. (1980), Late Quaternary sea level change on south Pacific coasts: A study in tectonic diversity, in *Earth Rheology, Isostasy, and Eustasy*, edited by N. A. Morner, pp. 505–516, Wiley-Interscience, New York.

Cooper, P., and B. Taylor (1987), Seismotectonics of New Guinea: A model for arc reversal following arc-continent collision, *Tectonics*, *6*, 53–67, doi:10.1029/TC006i001p00053.

D'Agostino, N., and G. Selvaggi (2004), Crustal motion along the Eurasia-Nubia plate boundary in the Calabrian Arc and Sicily and active extension in the Messina Straits from GPS measurements, *J. Geophys. Res.*, *109*, B11402, doi:10.1029/2004JB002998.

De Mets, C., R. G. Gordon, and D. F. Argus (2010), Geologically current plate motions, *Geophys. J. Intern.*, *181*, 1–80.

Dominguez, S., S. E. Lallemand, J. Malavieille, and R. von Huene (1998), Upper plate deformation associated with seamount subduction, *Tectonophysics*, *293*, 207–224.

Fisher, D., T. Gardner, J. Marshall, P. Sak, and M. Protti (1998), The effects of subducting seafloor roughness on forearc kinematics, Pacific coast, Costa Rica, *Geology*, *26*, 467–470.

Gallen, S. F., F. J. Pazzaglia, K. W. Wegmann, J. L. Pederson, and T. W. Gardner (2015), The dynamic reference frame of rivers and apparent transience in incision rates, *Geology*, *43*, 623–626.

Gardner, T. W., D. W. Jorgensen, C. Shuman, and C. R. Lemieux (1987), Geomorphic and tectonic process rates: Effects of measured time interval, *Geology*, *15*, 259–261.

Goldfinger, C., et al. (2012), Turbidite event history: Methods and implications for Holocene paleoseismicity of the Cascadia Subduction Zone, *U.S. Geol. Surv. Prof. Pap. 1661-F*, 170 pp.

Hetzel, R., and A. Hampel (2005), Slip rate variations on normal faults during glacial-interglacial changes in surface loads, *Nature*, *435*, 81–84.

James, S. T., J. J. Clague, K. Wang, and I. Hutchinson (2000), Postglacial rebound at the northern Cascadia subduction zone, *Quatern. Sci. Rev.*, *19*, 1527–1541.

Jerolmack, D. J., and P. M. Sadler (2007), Transience and persistence in the depositional record of continental margins, *J. Geophys. Res.*, *112*, F03S13, doi:10.1029/2006JF000555.

Kemp, D. B., and P. M. Sadler (2014), Climatic and eustatic signals in a global compilation of shallow marine carbonate accumulation rates, *Sedimentology*, *61*, 1286–1297.

Kulkarni, R., I. Wong, J. Zachariasen, C. Goldfinger, and M. Lawrence (2013), Statistical analyses of great earthquake recurrence along the Cascadia subduction zone, *Seismol. Soc. Am. Bull.*, *103*, 3205–3221, doi:10.1785/0120120105.

Laborel, J., C. Morhange, R. Lafont, J. L. Campion, F. Laborel-Deguen, and S. Sartoretto (1994), Biological evidence of sea-level rise during the last 4500 years on the rocky coasts of continental southwestern France and Corsica, *Mar. Geol.*, *120*, 203–223.

Lallemand, S., J. Malavieille, and S. Calassou (1992), Effects of oceanic ridge subduction on accretionary wedges, *Tectonics*, *11*, 1301–1313, doi:10.1029/92TC00637.

Lallemand, S. E., P. Schnurle, and J. Malavieille (1994), Coulomb theory applied to accretionary and nonaccretionary wedges—Possible causes for tectonic erosion and/or frontal accretion, *J. Geophys. Res.*, *99*, 12,033–12,055, doi:10.1029/94JB00124.

Mai, P. M., and G. C. Beroza (2002), A spatial random field model to characterize complexity in earthquake slip, *J. Geophys. Res.*, *107*(B11), 2308, doi:10.1029/2001JB000588.

Marco, S., M. Stein, and A. Agnon (1996), Long-term earthquake clustering: A 50,000-year paleoseismic record in the Dead Sea Graben, *J. Geophys. Res.*, *101*(B3), 6179–6191, doi:10.1029/95JB01587.

Masson, F., M. Anvari, Y. Djamour, A. Walpersdorf, F. Tavakoli, M. Daignieres, H. Nankali, and S. Van Gorp (2007), Large-scale velocity field and strain tensor in Iran inferred from GPS measurements; new insight for the present-day deformation pattern within NE Iran, *Geophys. J. Intern.*, *170*, 436–440.

Matthews, M. V., W. L. Ellsworth, and P. A. Reasenberg (2002), A Brownian model for recurrent earthquakes, *Bull. Seismol. Soc. Am.*, *92*, 2233–2250.

McCaffrey, R. (1997), Influences of recurrence times and fault zone temperatures on the age-rate dependence of subduction zone seismicity, *J. Geophys. Res.*, *102*, 22,839–22,854, doi:10.1029/97JB01827.

Meghraoui, M., S. Mechernich, E. Cetin, T. Haraguchi, M. Ferry, K. Okumura, S. Toda, and H. Tsutsumi (2013), The PALET project: Paleoseismology, paleotsunamis and uplift rates of NE Japan and their relationship to the earthquake cycle: *EGU Gen. Ass.*, *15*, EGU2013-5904, 2013.

Melnick, D., B. Bookhagen, M. R. Strecker, and H. P. Echtler (2009), Segmentation of megathrust rupture zones from forearc deformation patterns over hundreds to millions of years, Arauco Peninsula, Chile, *J. Geophys. Res.*, *114*, B01407, doi:10.1029/2008JB005788.

Moreno, M., M. Rosenau, and O. Oncken (2010), 2010 Maule earthquake slip correlates with pre-seismic locking of Andean subduction zone, *Nature*, *467*, 198–202.

Mouslopoulou, V., J. J. Walsh, and A. Nicol (2009), Fault displacement rates over a range of timescales, *Earth Planet. Sci. Lett.*, *278*, 186–197.

Mouslopoulou, V., J. Begg, A. Nicol, O. Oncken, and C. Prior (2015a), Formation of Late Quaternary paleoshorelines in Crete, Eastern Mediterranean, *Earth Planet. Sci. Lett.*, *431*, 294–307.

Mouslopoulou, V., A. Nicol, J. Begg, O. Oncken, and M. Moreno (2015b), Clusters of mega-earthquakes on upper plate faults control the Eastern Mediterranean hazard, *Geophys. Res. Lett.*, *42*, 10,282–10,289, doi:10.1002/2015GL066371.

Nicol, A., and J. Beavan (2003), Shortening of an overriding plate and its implications for slip on a subduction thrust, central Hikurangi Margin, New Zealand, *Tectonics*, *22*(6), 1070, doi:10.1029/2003TC001521.

Nicol, A., J. J. Walsh, K. Berryman, and P. Villamor (2006), Interdependence of fault displacement rates and paleoearthquakes in an active rift, *Geology*, *34*, 865–868.

Nicol, A., J. J. Walsh, V. Mouslopoulou, and P. Villamor (2009), Earthquake histories and Holocene acceleration of fault displacement rates, *Geology*, *37*, 911–914.
Ogata, Y. (1988), Statistical models for earthquake occurrence and residual analysis for point processes, *J. Am. Stat. Assoc.*, *83*, 9–27.
Okada, Y. (1992), Internal deformation due to shear and tensile faults in a half-space, *Bull. Seismol.Soc. Am.*, *82*, 1018–1040.
Ota, Y. (1986), Marine terraces as reference surfaces in late Quaternary tectonic studies: Examples from the Pacific Rim, *Bull. R. Soc. N. Z.*, *24*, 357–375.
Ota, Y., and M. Yamaguchi (2004), Holocene coastal uplift in the western Pacific Rim in the context of late Quaternary uplift, *Quatern. Intern.*, *120*, 105–117.
Park, J. O., T. Tsuru, S. Kodaira, P. R. Cummins, and Y. Kaneda (2002), Splay fault branching along the Nankai subduction zone, *Science*, *297*, 1157–1160.
Pedoja, K., et al. (2014), Coastal staircase sequences reflecting sea-level oscillations and tectonic uplift during the Quaternary and Neogene, *Earth Sci. Rev.*, *132*, 13–38.
Pinegina, T. K., J. Bourgeois, E. A. Kravchunovskaya, A. V. Lander, M. E. M. Arcos, K. Pedoja, and B. T. MacInnes (2013), A nexus of plate interaction: Vertical deformation of Holocene wave-built terraces on the Kamchatsky Peninsula (Kamchatka, Russia), *Geol. Soc. Am. Bull.*, *125*, 1554–1568.
Pirazzoli, P. A., J. Laborel, and S. C. Stiros (1996), Earthquake clustering in the Eastern Mediterranean during historical times, *J. Geophys. Res.*, *101*(B3), 6083–6097, doi:10.1029/95JB00914.
Priest, G. R., C. Goldfinger, K. Wang, R. C. Witter, Y. Zhang, and A. M. Baptista (2009), Confidence levels for tsunami-inundation limits in northern Oregon inferred from a 10,000-year history of great earthquakes at the Cascadia subduction zone, *Nat. Hazards*, *54*, 27–73.
Rajendran, C. P., K. Rajendran, M. Shah-hosseini, A. Naderi Beni, C. M. Nautiyal, and R. Andrews (2013), The hazard potential of the western segment of the Makran subduction zone, northern Arabian Sea, *Nat. Hazards*, *65*, 219–239.
Rodgers, D. W., and T. A. Little (2006), World's largest coseismic strike-slip offset: The 1855 rupture of the Wairarapa Fault, New Zealand, and implications for displacement/length scaling of continental earthquakes, *J. Geophys. Res.*, *111*, B12408, doi:10.1029/2005JA011505.
Rosenau, M., and O. Oncken (2009), Fore-arc deformation controls frequency-size distribution of megathrust earthquakes in subduction zones, *J. Geophys. Res.*, *114*, B10311, doi:10.1029/2009JB006359.
Rosenau, M., J. Lohrmann, and O. Oncken (2009), Shocks in a box: An analog model of subduction earthquake cycles with application to seismotectonic forearc evolution, *J. Geophys. Res.*, *114*, B01409, doi:10.1029/2008JB005665.
Ruff, L., and H. Kanamori (1980), Seismicity and the subduction process, *Phys. Earth Planet. Inter.*, *23*, 240–252.
Sadler, P. M. (1981), Sediment accumulation rates and the completeness of stratigraphic sections, *J. Geol.*, 569–584.
Sadler, P. M. (1994), The expected duration of upward-shallowing peritidal carbonate cycles and their terminal hiatuses, *Geol. Soc. Am. Bull.*, *106*, 791–802.
Sadler, P. M. (1999), The influence of hiatuses on sediment accumulation rates, *GeoRes. Forum*, *5*, 15–40.
Sadler, P. M., and D. J. Jerolmack (2014), Scaling laws for aggradation, denudation and progradation rates: The case for time-scale invariance at sediment sources and sinks, *Geol. Soc. Spec. Publ.*, *404*, 69–88.
Sadler, P. M., and D. J. Strauss (1990), Estimation of completeness of stratigraphical sections using empirical data and theoretical models, *J. Geol. Soc.*, *147*, 471–485.
Savage, J. C. (1983), A dislocation model of strain accumulation and release at a subduction zone, *J. Geophys. Res.*, *88*, 4984–4996, doi:10.1029/JB088iB06p04984.
Shaw, B., N. N. Ambraseys, P. C. England, M. A. Floyd, G. J. Gorman, T. F. G. Higham, J. A. Jackson, J. M. Nocquet, C. C. Pain, and M. D. Piggott (2008), Eastern Mediterranean tectonics and tsunami hazard inferred from the AD 365 earthquake, *Nat. Geosci.*, *1*, 268–276.
Siddall, M., E. J. Rohling, A. Almogi-Labin, C. Hemleben, D. Meischner, I. Schmelzer, and D. A. Smeed (2003), Sea-level fluctuations during the last glacial cycle, *Nature*, *423*, 853–858.
Sieh, K., D. H. Natawidjaja, A. J. Meltzner, C. C. Shen, H. Cheng, K. S. Li, B. W. Suwargadi, J. Galetzka, B. Philibosian, and R. L. Edwards (2008), Earthquake supercycles inferred from sea-level changes recorded in the corals of West Sumatra, *Science*, *322*, 1674–1678.
Singh, S. C., N. D. Hanando, and A. P. S. Chauhan (2011), Enhanced reflectivity of backthrusts in the recent great Sumatran earthquake rupture zones, *Geophys. Res. Lett.*, *38*, L04302, doi:10.1029/2010GL046227.
Stiros, S. (2010), The 8.5+ magnitude, AD 365 earthquake in Crete: Coastal uplift, topography changes and archaeological and historical signature, *Quatern. Intern.*, *216*, 54–63, doi:10.1016/j.quaint.2009.05.005.
Strauss, D., and P. M. Sadler (1989), Stochastic models for the completeness of stratigraphic sections, *Math. Geol.*, *21*, 37–59.
Suppe, J. (1981), Mechanics of mountain building and metamorphism in Taiwan, *Mem. Geol. Soc. China*, *4*, 67–89.
Tichelaar, B. W., and L. J. Ruff (1993), Depth of seismic coupling along subduction zones, *J. Geophys. Res.*, *98*(B2), 2017–2037, doi:10.1029/92JB02045.
Vernant, P., R. Reilinger, and S. McClusky (2014), Geodetic evidence for low coupling on the Hellenic subduction plate interface, *Earth Planet. Sci. Lett.*, *385*, 122–129.
Victor, P., M. Sobiesiak, S. Nielsen, J. Glodny, and O. Oncken (2011), Long-term persistence of subduction earthquake segment boundaries—Evidence from Mejillones Peninsula, N-Chile, *J. Geophys. Res.*, *116*, B02402, doi:10.1029/2010JB007771.
von Huene, R., and D. W. Scholl (1991), Observations at convergent margins concerning sediment subduction, subduction erosion, and the growth of continental crust, *Rev. Geophys.*, *29*, 279–316, doi:10.1029/91RG00969.
Wallace, L. M., J. Beavan, R. McCaffrey, and D. Darby (2004), Subduction zone coupling and tectonic block rotation in the North Island, New Zealand, *J. Geophys. Res.*, *109*, B12406, doi:10.1029/2004JB003241.
Wang, K. (2007), Elastic and viscoelastic models of crustal deformation in subduction earthquake cycles, in *The Seismogenic Zone of Subduction Thrust Faults*, edited by T. Dixon and J. C. Moore, pp. 540–575, Columbia Univ. Press, New York.
Wech, A. G., and C. Creager (2008), A continuum of stress, strength and slip in the Cascadia subduction zone, *Nat. Geosci.*, *4*, 624–628.
Willenbring, J., and F. von Blanckenburg (2010), Long-term stability of global erosion rates and weathering during late-Cenozoic cooling, *Nature*, *465*(7295), 211–214.
Wilson, K., K. Berryman, U. Cochran, and T. Little (2007), Holocene coastal evolution and uplift mechanisms of the northeastern Raukumara Peninsula, North Island, New Zealand, *Quatern. Sci. Rev.*, *26*, 1106–1128.
Wilson, K. J., K. R. Berryman, N. J. Litchfield, and T. Little (2006), A revision of mid-late Holocene marine terrace distribution and chronology at the Pakarae River mouth, North Island, New Zealand, *N. Z. J. Geol. Geophys.*, *49*, 477–489.
Zhuang, J., D. Harte, M. J. Werner, S. Hainzl, and S. Zhou (2012), Basic models of seismicity: Temporal models, *Commun. Online Resour. Stat. Seism. Anal.*, doi:10.5078/corssa-79905851. [Available at http://www.corssa.org.]